

PSR J1907+0602: A Radio-Faint Gamma-Ray Pulsar Powering a Bright TeV Pulsar Wind Nebula

A. A. Abdo^{2,3,1}, M. Ackermann⁴, M. Ajello⁴, L. Baldini⁵, J. Ballet⁶, G. Barbiellini^{7,8},
D. Bastieri^{9,10}, B. M. Baughman¹¹, K. Bechtol⁴, R. Bellazzini⁵, B. Berenji⁴,
R. D. Blandford⁴, E. D. Bloom⁴, E. Bonamente^{12,13}, A. W. Borgland⁴, J. Bregeon⁵,
A. Brez⁵, M. Brigida^{14,15}, P. Bruel¹⁶, T. H. Burnett¹⁷, S. Buson¹⁰, G. A. Caliandro^{14,15},
R. A. Cameron⁴, F. Camilo¹⁸, P. A. Caraveo¹⁹, J. M. Casandjian⁶, C. Cecchi^{12,13},
Ö. Çelik^{20,21,22}, A. Chekhtman^{2,23}, C. C. Cheung²⁰, J. Chiang⁴, S. Ciprini^{12,13}, R. Claus⁴,
I. Cognard²⁴, J. Cohen-Tanugi²⁵, L. R. Cominsky²⁶, J. Conrad^{27,28,29}, S. Cutini³⁰,
A. de Angelis³¹, F. de Palma^{14,15}, S. W. Digel⁴, B. L. Dingus³², M. Dormody³³,
E. do Couto e Silva⁴, P. S. Drell⁴, R. Dubois⁴, D. Dumora^{34,35}, C. Farnier²⁵, C. Favuzzi^{14,15},
S. J. Fegan¹⁶, W. B. Focke⁴, P. Fortin¹⁶, M. Frailis³¹, P. C. C. Freire^{36,63}, Y. Fukazawa³⁷,
S. Funk⁴, P. Fusco^{14,15}, F. Gargano¹⁵, D. Gasparrini³⁰, N. Gehrels^{20,38}, S. Germani^{12,13},
G. Giavitto³⁹, B. Giebels¹⁶, N. Giglietto^{14,15}, F. Giordano^{14,15}, T. Glanzman⁴, G. Godfrey⁴,
I. A. Grenier⁶, M.-H. Grondin^{34,35}, J. E. Grove², L. Guillemot^{34,35}, S. Guiriec⁴⁰,
Y. Hanabata³⁷, A. K. Harding²⁰, E. Hays²⁰, R. E. Hughes¹¹, M. S. Jackson^{27,28,41},
G. Jóhannesson⁴, A. S. Johnson⁴, T. J. Johnson^{20,38}, W. N. Johnson², S. Johnston⁴²,
T. Kamae⁴, H. Katagiri³⁷, J. Kataoka^{43,44}, N. Kawai^{43,45}, M. Kerr¹⁷, J. Knödlseeder⁴⁶,
M. L. Kocian⁴, M. Kuss⁵, J. Lande⁴, L. Latronico⁵, M. Lemoine-Goumard^{34,35}, F. Longo^{7,8},
F. Loparco^{14,15}, B. Lott^{34,35}, M. N. Lovellette², P. Lubrano^{12,13}, A. Makeev^{2,23},
M. Marelli¹⁹, M. N. Mazziotta¹⁵, J. E. McEnery²⁰, C. Meurer^{27,28}, P. F. Michelson⁴,
W. Mitthumsiri⁴, T. Mizuno³⁷, A. A. Moiseev^{21,38}, C. Monte^{14,15}, M. E. Monzani⁴,
A. Morselli⁴⁷, I. V. Moskalenko⁴, S. Murgia⁴, P. L. Nolan⁴, J. P. Norris⁴⁸, E. Nuss²⁵,
T. Ohsugi³⁷, N. Omodei⁵, E. Orlando⁴⁹, J. F. Ormes⁴⁸, D. Paneque⁴, D. Parent^{34,35},
V. Pelassa²⁵, M. Pepe^{12,13}, M. Pesce-Rollins⁵, F. Piron²⁵, T. A. Porter³³, S. Rainò^{14,15},
R. Rando^{9,10}, P. S. Ray², M. Razzano⁵, A. Reimer^{50,4}, O. Reimer^{50,4}, T. Reposeur^{34,35},
S. Ritz³³, M. S. E. Roberts^{2,23,51,1}, L. S. Rochester⁴, A. Y. Rodriguez⁵², R. W. Romani⁴,
M. Roth¹⁷, F. Ryde^{41,28}, H. F.-W. Sadrozinski³³, D. Sanchez¹⁶, A. Sander¹¹,
P. M. Saz Parkinson^{33,1}, J. D. Scargle⁵³, C. Sgrò⁵, E. J. Siskind⁵⁴, D. A. Smith^{34,35},
P. D. Smith¹¹, G. Spandre⁵, P. Spinelli^{14,15}, M. S. Strickman², D. J. Suson⁵⁵, H. Tajima⁴,
H. Takahashi³⁷, T. Tanaka⁴, J. B. Thayer⁴, J. G. Thayer⁴, G. Theureau²⁴,
D. J. Thompson²⁰, L. Tibaldo^{9,6,10}, O. Tibolla⁵⁶, D. F. Torres^{57,52}, G. Tosti^{12,13},
A. Tramacere^{4,58}, Y. Uchiyama^{59,4}, T. L. Usher⁴, A. Van Etten⁴, V. Vasileiou^{20,21,22},
C. Venter^{20,60}, N. Vilchez⁴⁶, V. Vitale^{47,61}, A. P. Waite⁴, P. Wang⁴, K. Watters⁴,
B. L. Winer¹¹, M. T. Wolff², K. S. Wood^{2,1}, T. Ylinen^{41,62,28}, M. Ziegler³³

¹Corresponding authors: A. A. Abdo, aous.abdo@nrl.navy.mil; M. S. E. Roberts, malloryr@gmail.com; P. M. Saz Parkinson, pablo@scipp.ucsc.edu; K. S. Wood, Kent.Wood@nrl.navy.mil.

²Space Science Division, Naval Research Laboratory, Washington, DC 20375, USA

³National Research Council Research Associate, National Academy of Sciences, Washington, DC 20001, USA

⁴W. W. Hansen Experimental Physics Laboratory, Kavli Institute for Particle Astrophysics and Cosmology, Department of Physics and SLAC National Accelerator Laboratory, Stanford University, Stanford, CA 94305, USA

⁵Istituto Nazionale di Fisica Nucleare, Sezione di Pisa, I-56127 Pisa, Italy

⁶Laboratoire AIM, CEA-IRFU/CNRS/Université Paris Diderot, Service d’Astrophysique, CEA Saclay, 91191 Gif sur Yvette, France

⁷Istituto Nazionale di Fisica Nucleare, Sezione di Trieste, I-34127 Trieste, Italy

⁸Dipartimento di Fisica, Università di Trieste, I-34127 Trieste, Italy

⁹Istituto Nazionale di Fisica Nucleare, Sezione di Padova, I-35131 Padova, Italy

¹⁰Dipartimento di Fisica “G. Galilei”, Università di Padova, I-35131 Padova, Italy

¹¹Department of Physics, Center for Cosmology and Astro-Particle Physics, The Ohio State University, Columbus, OH 43210, USA

¹²Istituto Nazionale di Fisica Nucleare, Sezione di Perugia, I-06123 Perugia, Italy

¹³Dipartimento di Fisica, Università degli Studi di Perugia, I-06123 Perugia, Italy

¹⁴Dipartimento di Fisica “M. Merlin” dell’Università e del Politecnico di Bari, I-70126 Bari, Italy

¹⁵Istituto Nazionale di Fisica Nucleare, Sezione di Bari, 70126 Bari, Italy

¹⁶Laboratoire Leprince-Ringuet, École polytechnique, CNRS/IN2P3, Palaiseau, France

¹⁷Department of Physics, University of Washington, Seattle, WA 98195-1560, USA

¹⁸Columbia Astrophysics Laboratory, Columbia University, New York, NY 10027, USA

¹⁹INAF-Istituto di Astrofisica Spaziale e Fisica Cosmica, I-20133 Milano, Italy

²⁰NASA Goddard Space Flight Center, Greenbelt, MD 20771, USA

²¹Center for Research and Exploration in Space Science and Technology (CRESST), NASA Goddard Space Flight Center, Greenbelt, MD 20771, USA

²²University of Maryland, Baltimore County, Baltimore, MD 21250, USA

²³George Mason University, Fairfax, VA 22030, USA

²⁴Laboratoire de Physique et Chimie de l’Environnement, LPCE UMR 6115 CNRS, F-45071 Orléans Cedex 02, and Station de radioastronomie de Nançay, Observatoire de Paris, CNRS/INSU, F-18330 Nançay,

France

²⁵Laboratoire de Physique Théorique et Astroparticules, Université Montpellier 2, CNRS/IN2P3, Montpellier, France

²⁶Department of Physics and Astronomy, Sonoma State University, Rohnert Park, CA 94928-3609, USA

²⁷Department of Physics, Stockholm University, AlbaNova, SE-106 91 Stockholm, Sweden

²⁸The Oskar Klein Centre for Cosmoparticle Physics, AlbaNova, SE-106 91 Stockholm, Sweden

²⁹Royal Swedish Academy of Sciences Research Fellow, funded by a grant from the K. A. Wallenberg Foundation

³⁰Agenzia Spaziale Italiana (ASI) Science Data Center, I-00044 Frascati (Roma), Italy

³¹Dipartimento di Fisica, Università di Udine and Istituto Nazionale di Fisica Nucleare, Sezione di Trieste, Gruppo Collegato di Udine, I-33100 Udine, Italy

³²Los Alamos National Laboratory, Los Alamos, NM 87545, USA

³³Santa Cruz Institute for Particle Physics, Department of Physics and Department of Astronomy and Astrophysics, University of California at Santa Cruz, Santa Cruz, CA 95064, USA

³⁴Université de Bordeaux, Centre d'Études Nucléaires Bordeaux Gradignan, UMR 5797, Gradignan, 33175, France

³⁵CNRS/IN2P3, Centre d'Études Nucléaires Bordeaux Gradignan, UMR 5797, Gradignan, 33175, France

³⁶Arecibo Observatory, Arecibo, Puerto Rico 00612, USA

³⁷Department of Physical Sciences, Hiroshima University, Higashi-Hiroshima, Hiroshima 739-8526, Japan

³⁸University of Maryland, College Park, MD 20742, USA

³⁹Istituto Nazionale di Fisica Nucleare, Sezione di Trieste, and Università di Trieste, I-34127 Trieste, Italy

⁴⁰University of Alabama in Huntsville, Huntsville, AL 35899, USA

⁴¹Department of Physics, Royal Institute of Technology (KTH), AlbaNova, SE-106 91 Stockholm, Sweden

⁴²Australia Telescope National Facility, CSIRO, Epping NSW 1710, Australia

⁴³Department of Physics, Tokyo Institute of Technology, Meguro City, Tokyo 152-8551, Japan

⁴⁴Waseda University, 1-104 Totsukamachi, Shinjuku-ku, Tokyo, 169-8050, Japan

⁴⁵Cosmic Radiation Laboratory, Institute of Physical and Chemical Research (RIKEN), Wako, Saitama 351-0198, Japan

⁴⁶Centre d'Étude Spatiale des Rayonnements, CNRS/UPS, BP 44346, F-30128 Toulouse Cedex 4, France

⁴⁷Istituto Nazionale di Fisica Nucleare, Sezione di Roma "Tor Vergata", I-00133 Roma, Italy

⁴⁸Department of Physics and Astronomy, University of Denver, Denver, CO 80208, USA

⁴⁹Max-Planck Institut für extraterrestrische Physik, 85748 Garching, Germany

ABSTRACT

We present multiwavelength studies of the 106.6 ms γ -ray pulsar PSR J1907+06 near the TeV source MGRO J1908+06. Timing observations with *Fermi* result in a precise position determination for the pulsar of R.A. = $19^{\text{h}}07^{\text{m}}54^{\text{s}}.7(2)$, decl. = $+06^{\circ}02'16(2)''$ placing the pulsar firmly within the TeV source extent, suggesting the TeV source is the pulsar wind nebula of PSR J1907+0602. Pulsed γ -ray emission is clearly visible at energies from 100 MeV to above 10 GeV. The phase-averaged power-law index in the energy range $E > 0.1$ GeV is $\Gamma = 1.76 \pm 0.05$ with an exponential cutoff energy $E_c = 3.6 \pm 0.5$ GeV. We present the energy-dependent γ -ray pulsed light curve as well as limits on off-pulse emission associated with the TeV source. We also report the detection of very faint (flux density of $\simeq 3.4 \mu\text{Jy}$) radio pulsations with the Arecibo telescope at 1.5 GHz having a dispersion measure $\text{DM} = 82.1 \pm 1.1 \text{ cm}^{-3}\text{pc}$. This indicates a distance of $3.2 \pm 0.6 \text{ kpc}$ and a pseudo-luminosity of $L_{1400} \simeq 0.035 \text{ mJy kpc}^2$. A *Chandra* ACIS observation revealed an absorbed, possibly extended, compact ($\lesssim 4''$) X-ray source with significant non-thermal emission at R.A. = $19^{\text{h}}07^{\text{m}}54^{\text{s}}.76$, decl. = $+06^{\circ}02'14.6''$ with a flux of $2.3_{-1.4}^{+0.6} \times 10^{-14} \text{ erg cm}^{-2}\text{s}^{-1}$. From archival *ASCA* observations, we place upper limits on any arcminute scale 2–10 keV X-ray emission of $\sim 1 \times 10^{-13} \text{ erg cm}^{-2}\text{s}^{-1}$. The implied distance to the pulsar is compatible with that of the supernova remnant G40.5–0.5, located on the far side of the TeV nebula from PSR J1907+0602, and the S74 molecular cloud on the nearer side which we discuss as potential birth sites.

Subject headings: pulsars: individual: PSR J1907+0602 — gamma rays: observations

1. Introduction

The TeV source MGRO J1908+06 was discovered by the Milagro collaboration at a median energy of 20 TeV in their survey of the northern Galactic Plane (Abdo et al. 2007) with a flux $\sim 80\%$ of the Crab at these energies. It was subsequently detected in the 300 GeV – 20 TeV range by the HESS (Aharonian et al. 2009) and VERITAS (Ward 2008) experiments. The HESS observations show the source HESS J1908+063 to be clearly extended, spanning $\sim 0.3^{\circ}$ of a degree on the sky with hints of energy-dependent substructure. A decade earlier Lamb & Macomb (1997) cataloged a bright source of GeV emission from the EGRET data, GeV J1907+0557, which is positionally consistent with MGRO J1908+06. It is near, but

⁵⁰Institut für Astro- und Teilchenphysik and Institut für Theoretische Physik, Leopold-Franzens-Universität Innsbruck, A-6020 Innsbruck, Austria

⁵¹Eureka Scientific, Oakland, CA 94602, USA

⁵²Institut de Ciències de l'Espai (IEEC-CSIC), Campus UAB, 08193 Barcelona, Spain

70 inconsistent with, the third EGRET catalog (Hartman et al. 1999) source 3EG J1903+0550
 71 (Roberts et al. 2001). The Large Area Telescope (LAT) (Atwood et al. 2009) aboard the
 72 *Fermi Gamma-Ray Space Telescope* has been operating in survey mode since soon after its
 73 launch on 2008 June 11, carrying out continuous observations of the GeV sky. The *Fermi*
 74 Bright Source List (Abdo et al. 2009b), based on 3 months of survey data, contains 0FGL
 75 J1907.5+0602 which is coincident with GeV J1907+0557. The 3EG J1903+0550 source loca-
 76 tion confidence contour stretches between 0FGL J1907.5+0602 and the nearby source 0FGL
 77 J1900.0+0356, suggesting it was a conflation of the two sources.

78 The *Fermi* LAT collaboration recently reported the discovery of 16 previously-unknown
 79 pulsars by using a time differencing technique on the LAT photon data above 300 MeV
 80 (Abdo et al. 2009a). 0FGL J1907.5+0602 was found to pulse with a period of 106.6 ms,
 81 have a spin-down energy of $\sim 2.8 \times 10^{36}$ erg s⁻¹, and was given a preliminary designation
 82 of PSR J1907+06. In this paper we derive a coherent timing solution using 14 months
 83 of data which yields a more precise position for the source, allowing detailed follow-up at
 84 other wavelengths, including the detection of radio pulsations using the Arecibo 305-m radio
 85 telescope. Energy resolved light curves, the pulsed spectrum, and off-pulse emission limits at
 86 the positions of the pulsar and PWN centroid are presented. We then report the detection of
 87 an X-ray counterpart with the *Chandra X-ray Observatory* and an upper limit from *ASCA*.
 88 Finally, we discuss the pulsar’s relationship to the TeV source and to the potential birth
 89 sites SNR G40.5–0.5 and the S74 HII region.

90 2. Gamma-ray Pulsar Timing and Localization

91 The discovery and initial pulse timing of PSR J1907+06 was reported by Abdo et al.
 92 (2009a). The source position used in that analysis (R.A. = 286.965°, Decl. = 6.022°) was
 93 derived from an analysis of the measured directions of LAT-detected photons in the on-pulse
 94 phase interval from observations made from 2008 August 4 through December 25. Here, we
 95 make use of a longer span of data and also apply improved analysis methods to derive an
 96 improved timing ephemeris for the pulsar as well as a more accurate source position.

97 For the timing and localization analysis, we selected “diffuse” class photons (events
 98 that passed the tightest background rejection criteria (Atwood et al. 2009)) with zenith
 99 angle $< 105^\circ$ as is standard practice and chose the minimum energy and extraction radius
 100 to optimize the significance of pulsations. We accepted photons with $E > 200$ MeV from
 101 within a radius of 0.7° of the nominal source direction. We corrected these photon arrival

102 times to terrestrial time (TT) at the geocenter using the LAT Science Tool ¹ `gtbary` in its
 103 geocenter mode.

104 We fitted a timing model using TEMPO2(Hobbs et al. 2006) to 23 pulse times of arrival
 105 (TOAs) covering the interval 2008 June 30 to 2009 September 18. We note that during
 106 the on-orbit checkout period (before 2008 August 4) several instrument configurations were
 107 tested that affected the energy resolution and event reconstruction but had no effect on the
 108 LAT timing. To determine the TOAs, we generated pulse profiles by folding the photon times
 109 according to a provisional ephemeris using polynomial coefficients generated by TEMPO2 in
 110 its predictive mode (assuming a fictitious observatory at the geocenter). The TOAs were
 111 measured by cross correlating each pulse profile with a kernel density template that was
 112 derived from fitting the full mission dataset (Ray et al. 2009). Finally, we fitted the TOAs
 113 to a timing model that included position, frequency, and frequency derivative. The resulting
 114 timing residuals are 0.4 ms and are shown in Figure 1. The best-fit model is displayed in
 115 Table 1. The numbers in parentheses are the errors in the last digit of the fitted parameters.
 116 The errors are statistical only, except for the position error, as described below. The derived
 117 parameters of \dot{E} , B , and τ_c are essentially unchanged with respect to those reported by
 118 Abdo et al. (2009a), but the position has moved by $1.2'$.

119 The statistical error on the position fit is $< 1''$; however, this is an underestimate of the
 120 true error. For example, with only one year of data, timing noise can perturb the position
 121 fit. We have performed a Monte Carlo analysis of these effects by simulating fake residuals
 122 using the FAKE plugin for TEMPO2. We generated models with a range of frequency second
 123 derivatives ($\pm 2 \times 10^{-22}\text{s}^{-3}$, the allowed magnitude for $\ddot{\nu}$ in our fits) to simulate the effects
 124 of timing noise and fitted them to timing models. Based on these simulations, we assigned
 125 an additional systematic error on the position of $2''$, which we added in quadrature to the
 126 statistical error in Table 1. As a result of the improved position estimate provided by this
 127 timing analysis, we have adopted a more precise name for the pulsar of PSR J1907+0602.

128 3. Detection of Radio Pulsations

129 To search for radio pulsations, we observed the timing position of PSR J1907+0602
 130 with the L-wide receiver on the Arecibo 305-m radio telescope. On 2009 August 21 we made
 131 a 55-minute pointing with center frequency 1.51 GHz and total bandwidth of 300 MHz,
 132 provided by three Wideband Arecibo Pulsar Processors (WAPPs, Dowd et al. (2000)), each
 133 individually capable of processing 100 MHz. We divided this band into 512-channel spectra

¹<http://fermi.gsfc.nasa.gov/ssc/data/analysis/documentation/index.html>

134 accumulated every 128 μs . The small positional uncertainty of PSR J1907+0602 derived from
 135 the LAT timing means that a single Arecibo pointing covers the whole region of interest.

136 After excising strong sources of radio-frequency interference with `rfifind`, one of the
 137 routines of the PRESTO signal analysis package (Ransom et al. 2002), we performed a search
 138 by folding the raw data with the *Fermi* timing model into 128-bin pulse profiles. We then
 139 used the PRESTO routine `prepfold` to search trial dispersion measures between 0 and 1000
 140 pc cm^{-3} . We found a pulsed signal with a signal-to-noise ratio $S/N = 9.4^2$ and duty cycle
 141 of about 0.03 at a dispersion measure $DM = 82.1 \pm 1.1 \text{ cm}^{-3} \text{ pc}$. This value was estimated
 142 by dividing the detection data into 3 sub-bands and making TOAs for each sub-band and
 143 fitting for the DM with TEMPO.

144 We applied the same technique for 4 different time segments of 12.5 minutes each and
 145 created a time of arrival for each of them. We then estimated the barycentric periodicity of
 146 the detected signal from these times of arrival. This differs from the periodicity predicted
 147 by the LAT ephemeris for the time of the observation by $(-0.000005 \pm 0.000020) \text{ ms}$, i.e.,
 148 the signals have the same periodicity.

149 Subsequent radio observations showed that the phase of the radio pulses is exactly as
 150 predicted by the LAT ephemeris, apart from a constant phase offset (depicted in Figure 2)

151 A confirmation observation with twice the integration time (1.8 hr) was made on 2009
 152 September 4. The radio profile is shown in the bottom panel of Figure. 2 with an arbitrary
 153 intensity scale. The pulsar is again detected with S/N of 3.4, 5.1, 7.3 and 8.6 at 1170, 1410,
 154 1510 and 1610 MHz. The higher S/N at the higher frequencies suggest a positive spectral
 155 index, similar to what has been observed for PSR J1928+1746 (Cordes et al. 2006). However,
 156 this might instead be due to scattering degrading the S/N at the lowest frequencies— for
 157 the band centered at 1610 MHz the pulse profile is distinctively narrower (about 2% at 50%
 158 power) than at 1410 or 1510 MHz (about 3%). At 1170 MHz the profile is barely detectable
 159 but very broad. This suggests an anomalously large scattering timescale for the DM of the
 160 pulsar. Observations at higher frequencies will settle the issue of the positive spectral index.
 161 For the 300 MHz centered at 1410 MHz, where the detection is clear, we obtain a total S/N
 162 of 12.4.

163 With an antenna $T_{\text{sys}} = 33 \text{ K}$ (given by the frequency-dependent antenna temperature of

²This was estimated using another software package, SIGPROC (a package developed by Duncan Lorimer, see <http://sigproc.sourceforge.net/>), which processes the bands separately and produced S/N of 4.2, 6.3 and 5.5 for the WAPPs centered at 1410, 1510 and 1610 MHz. Although $S/N = 9.4$ is close to the detection threshold for pulsars in a blind search, it is much more significant in this case because of the reduced number of trials in this search relative to a blind search.

164 25–27 K off the plane of the Galaxy plus 6 K of Galactic emission in the specific direction of
 165 the pulsar (Haslam et al. 1982), Gain = 10.5 K Jy⁻¹ and 2 polarizations, and an inefficiency
 166 factor of 12% due to the 3-level sampling of the WAPP correlators, we obtain for the first
 167 detection a flux density at 1.4 GHz of $S_{1400} \simeq 4.1 \mu\text{Jy}$ and for the second detection $S_{1400} \simeq$
 168 $3.1 \mu\text{Jy}$. These values are consistent given the large relative uncertainties in the S/N estimates
 169 and the varying effect of radio frequency interference; at this DM, scintillation is not likely
 170 to cause a large variation in the flux density.

171 The time-averaged flux density is $\simeq 3.4 \mu\text{Jy}$. Using the NE2001 model for the electron
 172 distribution in the Galaxy (Cordes & Lazio 2002), we obtain from the pulsar’s position and
 173 DM a distance of 3.2 kpc with a nominal error of 20% (Cordes & Lazio 2002). The time-
 174 averaged flux density thus corresponds to a pseudo-luminosity $L_{1400} \simeq 0.035 \text{ mJy kpc}^2$. This
 175 is fainter than the least luminous young pulsar in the ATNF catalog (PSR J0205+6449, with
 176 a 1.4 GHz pseudo-luminosity of 0.5 mJy kpc^2). It is, however, more luminous than the radio
 177 pulsations discovered through a deep search of another pulsar first discovered by Fermi, PSR
 178 J1741–2054 which has $L_{1400} \sim 0.025 \text{ mJy kpc}^2$ (Camilo et al. 2009). These two detections
 179 clearly demonstrate that some pulsars, as seen from the Earth, can have extremely low
 180 apparent radio luminosities; i.e., similarly deep observations of other γ -ray selected pulsars
 181 might detect additional very faint radio pulsars. We note that these low luminosities, which
 182 may well be the result of only a faint section of the radio beam crossing the Earth, are much
 183 lower than what has often been termed “radio quiet” in population synthesis models used to
 184 estimate the ratio of “radio-loud” to “radio quiet” γ -ray pulsars (eg. Gonthier et al. 2004).

185 4. Energy-Dependent Gamma-ray Pulse Profiles

186 The pulse profile and spectral results reported in this paper use the survey data collected
 187 with the LAT from 2008 August 4 through 2009 September 18. We selected “diffuse” class
 188 photons (see §2) with energies $E > 100 \text{ MeV}$ and, to limit contamination from photons from
 189 Earth’s limb, with zenith angle $< 105^\circ$.

190 To explore the dependence of the pulse profile on energy, we selected an energy-dependent
 191 region of interest (ROI) with radius $\theta = 0.8 \times E^{-0.75}$ degrees, but constrained not to be out-
 192 side the range $[0.35^\circ, 1.5^\circ]$. We chose the upper bound to minimize the contribution from
 193 nearby sources and Galactic diffuse emission. The lower bound was selected in order to in-
 194 clude more photons from the wings of the point spread function (PSF) where the extraction
 195 region is small enough to make the diffuse contribution negligible. Figure 2 shows folded
 196 light curves of the pulsar in 32 constant-width bins for different energy bands. We use the
 197 centroid of the 1.4 GHz radio pulse profile to define phase 0.0. Two rotations are shown in

198 each case. The top panel of the figure shows the folded light curve for photons with $E > 0.1$
 199 GeV. The γ -ray light curve shows two peaks, P1 at phase 0.220 ± 0.002 which determines
 200 the offset with the radio peak, δ . The second peak in the γ -ray, P2, occurs at phase 0.580
 201 ± 0.003 . The phase separation between the two peaks is $\Delta = 0.360 \pm 0.004$. The radio
 202 lead δ and gamma peak separation Δ values are in good agreement with the correlation
 203 predicted for outer magnetosphere models, (Romani & Yadigaroglu 1995) and observed for
 204 other young pulsars (Figure 3 of Abdo et al. (2009c)).

205 Pulsed emission from the pulsar is clearly visible for energies $E > 5$ GeV with a chance
 206 probability of $\sim 4 \times 10^{-8}$. Pulsed emission is detected for energies above 10 GeV with a
 207 confidence level of 99.8%. We have measured the integral and widths of the peaks as a
 208 function of energy and have found no evidence for significant evolution in shape or P1/P2
 209 ratio with energy. We note that the pulsar is at low Galactic latitude ($b \sim -0.89^\circ$) where
 210 the Galactic γ -ray diffuse emission is bright (it has not been subtracted from the light curves
 211 shown.)

212 Figure 3 shows the observed LAT counts map of the region around PSR J1907+0602.
 213 We defined the “on” pulse as pulse phases $0.12 \leq \phi \leq 0.68$ and the “off” pulse as its
 214 complement ($0.0 \leq \phi < 0.12$ and $0.68 < \phi \leq 1.0$). We produced on-pulse (left panel) and
 215 off-pulse (right panel) images, scaling the off-pulse image by 1.27. The figure indicates the
 216 complexity of the region that must be treated in spectral fitting. Besides the pulsar there
 217 are multiple point sources, Galactic, and extragalactic diffuse contributions.

218 5. Energy Spectrum

219 The phase-averaged flux of the pulsar was obtained by performing a maximum likelihood
 220 spectral analysis using the *Fermi* LAT science tool `gtlike`. Starting from the same data set
 221 described in §4, we selected photons from an ROI of 10 degrees around the pulsar position.
 222 Sources from a preliminary version (based on 11 months of data) of the first *Fermi* LAT
 223 γ -ray catalog (Abdo et al. 2009c) that are within 15 degree ROI around the pulsar were
 224 modeled in this analysis. Spectra of sources farther away than 5° from the pulsar were fixed
 225 at the cataloged values. Sources within 5° degrees of the pulsar were modeled with a simple
 226 power law. For each of the sources in the 5° degree region around the pulsar, we fixed the
 227 spectral index at the value in the catalog and fitted for the normalization. Two sources
 228 that are at a distance $> 5^\circ$ showed strong emission and were treated the same way as the
 229 sources within 5° . The Galactic diffuse emission (gll_iemv02) and the extragalactic diffuse

230 background (isotropic_iem_v02) were modeled as well³.

The assumed spectral model for the pulsar is an exponentially cut-off power law: $dN/dE = N_o (E/E_o)^{-\Gamma} \exp(-E/E_c)$. The resulting spectrum gives the total emission for the pulsar assuming that the γ -ray emission is 100% pulsed. The unbinned `gtlike` fit, using P6_v3 instrument response functions (Atwood et al. 2009), for the energy range $E \geq 100$ MeV gives a phase-averaged spectrum of the following form:

$$\frac{dN}{dE} = (7.06 \pm 0.43_{stat.} + {}^{(+0.004)}_{(-0.064)}_{sys.}) \times 10^{-11} E^{-\Gamma} e^{-E/E_c} \gamma \text{ cm}^{-2} \text{ s}^{-1} \text{ MeV}^{-1} \quad (1)$$

231 where the photon index $\Gamma = 1.76 \pm 0.05_{stat.} + {}^{(+0.271)}_{(-0.287)}_{sys.}$ and the cutoff energy $E_c = 3.6 \pm$
 232 $0.5_{stat.} + {}^{(+0.72)}_{(-0.36)}_{sys.}$ GeV.

233 The integrated energy flux from the pulsar in the energy range $E \geq 100$ MeV is $F_\gamma =$
 234 $(3.12 \pm 0.15_{stat.} + {}^{(+0.16)}_{(-0.15)}_{sys.}) \times 10^{-10} \text{ ergs cm}^{-2} \text{ s}^{-1}$. This yields a γ -ray luminosity of $L_\gamma =$
 235 $4\pi f_\Omega F_\gamma d^2 = 3.8 \times 10^{35} f_\Omega d_{3.2}^2 \text{ ergs s}^{-1}$ above 100 MeV, where f_Ω is an effective beaming factor
 236 and $d_{3.2} = d/(3.2) \text{ kpc}$. This corresponds to an efficiency of $\eta = L_\gamma/\dot{E} = 0.13 F_\gamma d_{3.2}^2$ for
 237 conversion of spin-down power into γ -ray emission in this energy band.

238 We set a 2σ flux upper limit on γ -ray emission from the pulsar in the off-pulse part
 239 of $F_{off} < 8.31 \times 10^{-8} \text{ cm}^{-2} \text{ s}^{-1}$. In addition to the γ -ray spectrum from the point-source
 240 pulsar PSR J1907+0602, we measured upper limits on γ -ray flux from the extended source
 241 HESS J1908+063 in the energy range 0.1–25 GeV. We performed binned likelihood analysis
 242 using the *Fermi* Science Tool `gtlike`. In this analysis we assumed an extended source
 243 with gaussian width of 0.3° and γ -ray spectral index of -2.1 at the location of the HESS
 244 source. The upper limits suggest that the spectrum of HESS J1908+063 has a low energy
 245 turnover between 20 GeV and 300 GeV. Figure 4 shows the phase-averaged spectral energy
 246 distribution for PSR J1907+0602 (green circles). On the same figure we show data points
 247 from HESS for the TeV source HESS J1908+063 (blue circles) and the 2σ upper limits from
 248 *Fermi* for emission from this TeV source. Figure 5 shows an off pulse residual map of the
 249 region around PSR J1907+0602. The timing position of the pulsar is marked by the green
 250 cross. The 5σ contours from Milagro (outer) and HESS (inner) are overlaid. As can be seen
 251 from the residual map, there is no gamma-ray excess at the location of either the pulsar or
 252 the PWN.

³Descriptions of the models are available at <http://fermi.gsfc.nasa.gov/>

6. X-ray Counterpart

253

254 A 23 ks *ASCA* GIS exposure of the EGRET source GeV J1907+0557 revealed an \sim
 255 $8' \times 15'$ region of possible extended hard emission surrounding two point-like peaks lying $\sim 15'$
 256 to the southwest of PSR J1907+0602 (Roberts et al. 2001) and no other significant sources
 257 in the $44'$ *ASCA* FOV. A 10 ks *Chandra* ACIS-I image of the *ASCA* emission (ObsID 7049)
 258 showed it to be dominated by a single hard point source, CXOU J190718.6+054858 with no
 259 compact nebular structure and just a hint of the several arcminute-scale emission seen by
 260 *ASCA*. CXOU J190718.6+054858 seemed to turn off for ~ 2 ks during the *Chandra* exposure,
 261 suggesting that it may be a binary of some sort or else a variable extragalactic source. There
 262 is no obvious optical counterpart in the digital sky survey optical or 2MASS near infrared
 263 images, nor in a I band image taken with the 2.4m Hiltner telescope at MDM (Jules Halpern,
 264 private communication). This strongly suggests that it is not a nearby source. An absorbed
 265 power law fits the spectrum of this source well, with absorption $n_H = 1.8_{-0.9}^{+1.3} \times 10^{22} \text{cm}^{-2}$
 266 (90% confidence region), a photon spectral index $\Gamma = 0.9_{-0.4}^{+0.6}$, and an average 2–10 keV flux
 267 of $4.4_{-1.8}^{+0.7} \times 10^{-13} \text{erg cm}^{-2} \text{s}^{-1}$ (68% confidence region). The fit absorption is similar to the
 268 estimated total Galactic absorption from the HEASARC *nH* tool of $1.6 \times 10^{22} \text{cm}^{-2}$ based
 269 on the Dickey and Lockman (1990) HI survey (Dickey & Lockman 1990), suggesting that
 270 an n_H of $\sim 2 \times 10^{22} \text{cm}^{-2}$ is a reasonably conservative estimate of interstellar absorption for
 271 sources deep in the plane along this line of sight.

272 The timing position of LAT PSR J1907+0602 is in the central $20'$ of the *ASCA* GIS
 273 FOV (Figure 6). There is no obvious emission in the *ASCA* image at the pulsar position.
 274 Using the methodology of Roberts et al. (2001), a 24 pixel radius extraction region ($\sim 6'$),
 275 and assuming an absorbed power law spectrum with $n_H = 2 \times 10^{22} \text{cm}^{-2}$ and $\Gamma = 1.5$, we
 276 place a 90% confidence upper limit on the 2–10 keV flux $F_x < 5 \times 10^{-14} \text{erg cm}^{-2} \text{s}^{-1}$. This
 277 suggests that for any reasonable absorption, the total unabsorbed X-ray flux from the pulsar
 278 plus any arcminute-scale nebula is less than $10^{-13} \text{erg cm}^{-2} \text{s}^{-1}$.

279 PSR J1907+0602 was well outside of the FOV of the first *Chandra* observation, and
 280 so we proposed for an observation centered on the pulsar. We obtained a 19 ks exposure
 281 with the ACIS-S detector (ObsID 11124). The time resolution of the ACIS-S detector on
 282 board *Chandra* does not allow for pulse studies. The only source within an arcminute
 283 of the timing position and the brightest source in the FOV of the S3 chip is shown in
 284 Figure 7. It is well within errors of the timing position. Examination of the X-ray image
 285 in different energy bands showed virtually no detected flux below $\sim 1 \text{keV}$ and significant
 286 flux above 2.5 keV, suggesting a non-thermal emission mechanism for much of the flux.
 287 A comparison of the spatial distribution of counts between 0.75 keV and 2 keV to those
 288 between 2keV and 8keV shows some evidence for spatial extent beyond the point spread

289 function for the harder emission but not for the softer emission. This would be consistent
 290 with an interpretation as predominantly absorbed but thermal emission from a neutron star
 291 surface surrounded by non-thermal emission from a compact pulsar wind nebula, which is
 292 the typical situation for young pulsars (see Kaspi et al. 2006, and references therein). We
 293 plot the *Chandra* 0.75-2keV, 2-8keV, and 0.75-8 keV images with an ellipse showing the
 294 timing position uncertainty, and a circle with a radius of $0.8''$. From a modeled PSF, we
 295 estimate 80% of the counts should be contained within this circle. While this seems to be
 296 the case for the soft image, only roughly half the counts in the harder image are contained
 297 within that radius. With only ~ 12 source counts in the 0.75-2 keV image within $6''$ and
 298 ~ 30 source counts in the 2-8 keV image, quantitative statements about source size and
 299 spectrum are difficult to make. We obtain a best fit position for the nominal point source of
 300 R.A. = $19^{\text{h}}07^{\text{m}}54^{\text{s}}.76$, decl. = $+06^{\circ}02'14.6''$ and estimated error of $0.7''$ (an additional $0.1''$
 301 centroid fitting uncertainty added to the nominal *Chandra* $0.6''$ uncertainty). Using a $6''$
 302 radius extraction region and an annulus between $6''$ and $24''$ for background, we extracted
 303 source and background spectra and fit them within XSPEC (Figure 8). A simple power law
 304 plus absorption model fit the data well in the energy range 2-10 KeV, with best fit values
 305 $n_H = 1.3 \times 10^{22} \text{cm}^{-2}$ and $\Gamma = 1.6$, with a total flux of $2.3_{-1.4}^{+0.6} \times 10^{-14} \text{erg cm}^{-2} \text{s}^{-1}$. The
 306 low count rates and covariance between the absorption and photon index meant the spectral
 307 parameters could not be simultaneously meaningfully constrained. Fixing the spectral index
 308 $\Gamma = 1.6$, a typical value for compact pulsar wind nebulae (Kaspi et al. 2006), we obtain a
 309 90% confidence region for the absorption of $0.7 - 2.5 \times 10^{22} \text{cm}^{-2}$, consistent with a source a
 310 few kilo parsecs or more away and with CXOU J190718.6+054858 discussed above. We note
 311 that with such an absorption a significant thermal component in the below 2 keV emission
 312 is neither required nor ruled out by the spectral fitting.

313 7. Discussion

314 The dispersion measure from the radio detection suggests a distance of 3.2 kpc, with
 315 a nominal error of 20%. However, there are many outliers to the DM error distribution,
 316 although the largest fractional errors tend to be from pulsars at high Galactic latitudes or
 317 very low DMs (Deller et al. 2009; Chatterjee et al. 2009). For PSR J1907+0602, at a latitude
 318 $b = -0.9^{\circ}$ with a moderate DM, the distance estimate is likely to be reasonable. Since the
 319 apparent γ -ray pulsed efficiency in the *Fermi* pass-band is well above the median for other
 320 gamma-ray pulsars in Abdo et al. (2009d) (13% compared to 7.5%), it is worth checking
 321 secondary distance indicators to see if the DM measure could be a significant overestimate
 322 of the true distance. We can use the X-ray observations of PSR J1907+0602 to do this.
 323 Several authors have noted a correlation between the X-ray luminosity of young pulsars and

324 their spin-down power (eg. Saito 1998, Possenti et al. 2002, Li, Lu and Li 2007). Most
 325 of these have the problem of using X-ray fluxes derived from the literature using a variety
 326 of instruments with no uniform way of choosing spectral extraction regions. This can be
 327 especially problematic with *Chandra* data, since faint, arcminute scale emission can easily be
 328 overlooked. We compare our *ASCA* GIS upper limits to Figure 1 of Cheng, Taam and Wang
 329 (2004) who used only *ASCA* GIS data to derive their X-ray luminosity relationships. We see
 330 that the typical X-ray luminosity in the *ASCA* band for a pulsar with $\dot{E} = 2 \times 10^{36} \text{erg s}^{-1}$
 331 is $L_x \sim 10^{33} - 10^{34} \text{erg s}^{-1}$ with all of the pulsars used in their analysis with $\dot{E} > 10^{36} \text{erg s}^{-1}$
 332 having $L_x > 10^{32} \text{erg s}^{-1}$. From these values and the *ASCA* upper limit, we derive a lower
 333 limit for the distance to LAT PSR J1907+0602 of ~ 3 kpc. From Figure 2 of Li, Lu and
 334 Li (2007), who used *XMM-Newton* and *Chandra* derived values, we see we can expect the
 335 luminosity to be between $\sim 10^{31.5} - 10^{34.5} \text{erg s}^{-1}$. From our detection with *Chandra*, we
 336 again estimate a lower distance limit of ~ 3 kpc. The “best guess” estimate from their
 337 relationship would result in a distance of ~ 13 kpc. We note that if we assume the pulsed
 338 emission to be apparently isotropic (i.e. $f_\Omega = 1$ as simple outer gap models suggest should
 339 approximately be the case, see Watters et al. (2009)), a distance of 9 kpc would result in
 340 100% γ -ray efficiency.

341 The derived timing position of PSR J1907+0602 is well inside the extended HESS source,
 342 although $\sim 14'$ southwest of the centroid. The TeV source is therefore plausibly the wind
 343 nebula of PSR J1907+0602. The physical size of this nebula is then $\gtrsim 40$ pc, and the
 344 integrated luminosity above 1 TeV is $\gtrsim 40\%$ that of the Crab, and in the MILAGRO band
 345 (~ 20 TeV) at least twice that of the Crab. There is a hint of some spatial dependence of
 346 the TeV spectrum in the HESS data, with the harder emission (> 2.5 TeV) peaking nearer
 347 the pulsar than the softer emission (Aharonian et al. 2009). If confirmed, this would be
 348 consistent with the hardening of the TeV emission observed towards PSR B1823–13, thought
 349 to be the pulsar powering HESS J1825–137 (Aharonian et al. 2006). This latter pulsar has
 350 a spin period, characteristic age, and spin-down energy similar to PSR J1907+0602, and
 351 is also located near the edge of its corresponding TeV nebula. We also note that HESS
 352 J1825–137 subtends $\sim 1^\circ$ on the sky and has a flux level above 1 TeV of around 20% of the
 353 Crab. While the overall spectrum of HESS J1825–137 is somewhat softer than the spectrum
 354 of HESS J1908+063, near the pulsar its spectrum is similarly hard. At a distance of ~ 4 kpc,
 355 HESS J1825–137 has a luminosity similar to the Crab TeV nebula, but with a much larger
 356 physical size of ~ 70 pc. Given the distance implied above and a flux above 1 TeV $\sim 17\%$ of
 357 the Crab, HESS J1908+063 is similar in size and luminosity to HESS J1825–137.

358 At 20 TeV, HESS J1908+063 has a flux $\sim 80\%$ of the Crab, and so at a distance $\gtrsim 1.5$
 359 times that of the Crab, is much more luminous at the highest energies. This is because there
 360 is no sign of a high-energy cutoff or break, as is seen in many other TeV nebulae. Aharonian

361 et al. (2009) place a lower limit of 19.1 TeV on any exponential cutoff to the spectrum.
 362 This implies that either the spectrum is uncooled due to a very low nebular magnetic field
 363 ($\lesssim 3\mu\text{G}$, see, eg. de Jager (2008)), an age much less than the characteristic age of 19.5 kyr,
 364 or else there is a synchrotron cooling break below the HESS band.

365 Our upper limits above a few GeV (Figure 4) requires there to be a low energy turnover
 366 between 20 GeV and 300 GeV. Given the nominal PWN spectrum, we constrain the overall
 367 PWN flux to be $\leq 25\%$ of that of the pulsar. If only the HESS band is considered, and
 368 assuming the DM distance, the TeV luminosity $L_{\text{PWN}} = 5 - 8\% \dot{E}$. However, since the TeV
 369 emission is generally thought to come from a relic population of electrons the luminosity is
 370 likely a function of the spin-down history of the pulsar rather than the current spin-down
 371 luminosity (eg. de Jager 2008). These numbers support consistency of the association of the
 372 TeV source with the pulsar, in the weak sense of not being discrepant with other similar
 373 systems.

374 7.1. On the possible association with SNR G40.5–0.5

375 The bulk of HESS J1908+063 is between PSR J1907+0602 and the young radio SNR
 376 G40.5–0.5, suggesting a possible association. The distance estimate (~ 3.4 kpc Yang et al.
 377 2006) and age (Downes et al. 1980) estimates of SNR G40.5–0.5 are also consistent with
 378 those of PSR J1907+0602. If we use the usually assumed location for SNR G40.5–0.5 given
 379 by Langston et al. (2000) (RA=19^h07^m11^s.9, Dec=6°35′15″), we get an angular separation of
 380 $\sim 35'$ between the timing position for the pulsar and the SNR. However, this position for the
 381 SNR is from single dish observations that were offset towards one bright side of the nominal
 382 shell. We use the VLA Galactic Plane Survey 1420 MHz image (Stil et al. 2006) of this region
 383 to estimate the SNR center to be RA=19^h07^m08^s.6, Dec=6°29′53″ (Figure 9) which, for an
 384 assumed distance of 3.2 kpc, would give a separation of ~ 28 pc. Given the characteristic age
 385 of 19.5 kyr years, this would require an average transverse velocity of ~ 1400 km/s. While
 386 velocities about this high are seen in some cases (eg. PSR B1508+55 has a transverse velocity
 387 of ~ 1100 km/s, Chatterjee et al. 2005), it is several times the average pulsar velocity and
 388 many times higher than the local sound speed. We note that pulsars with a braking index
 389 significantly less than $n = 3$ assumed in the derivation of the characteristic age could have
 390 ages as much as a factor of two greater (see eg. Kaspi et al. 2001), and thus a space velocity
 391 around half the above value may be all that is required. But with any reasonable assumption
 392 of birthplace, distance, and age, if the pulsar was born in SNR G40.5–0.5, any associated
 393 X-ray or radio PWN should show a bow-shock and trail morphology, with the trail likely
 394 pointing back towards the SNR center. Unfortunately, the compactness and low number of

395 counts in our *Chandra* image precludes any definite statement about the PWN morphology.
396 One arrives at a different, and lower, minimum velocity if one assumes the pulsar was born
397 at the center of the TeV PWN and moved to its present position, but the resulting velocity
398 would still require a bow shock.

399 One can also get a pulsar offset towards the edge of a relic PWN if there is a significant
400 density gradient in the surrounding ISM. A gradient will cause the supernova blast wave to
401 propagate asymmetrically. Where the density is higher, the reverse shock propagating back
402 to the explosion center will also be asymmetric. This will tend to push the PWN away from
403 the region of higher density (Blondin et al. 2001; Ferreira & de Jager 2008). This has been
404 invoked to explain the offsets in the Vela X and HESS J1825–137 nebulae as well as several
405 others. Infrared and radio imaging of the region shows that HESS J1908+063 borders on
406 a shell of material surrounding the S74 HII region, also known as the Lynds Bright Nebula
407 352. Russeil (2003) gives a kinematic distance of 3.0 ± 0.3 kpc for this star forming region,
408 compatible with the pulsar distance. In this scenario, the pulsar would not have to be highly
409 supersonic to be at the edge of a relic nebula, and would not have to be traveling away from
410 the center of the TeV emission.

411 A third, hybrid possibility is that SNR G40.5–0.5 is only a bright segment of a much
412 larger remnant, whose emission from the side near the pulsar is confused with that from the
413 molecular cloud. The asymmetry would be explained by the difference in propagation speed
414 in the lower density ISM away from the molecular cloud.

415 Our current *Chandra* data are insufficient to distinguish between the above scenarios.
416 However, there is also the possibility of a compact cometary radio nebula, such as is seen
417 around PSR B1853+01 in SNR W44 (Frail et al. 1996) and PSR B0906–49 (Gaensler et al.
418 1998). In addition, sensitive long wavelength radio imaging could reveal any larger, faint
419 SNR shells. Imaging with the EVLA and LOFAR of this region is therefore highly desirable.
420 The connection between the pulsar and the TeV nebula could be further strengthened by a
421 confirmation of the spatio-spectral dependence of the nebula where the spectrum hardens
422 nearer to the pulsar.

423 The *Fermi* LAT Collaboration acknowledges the generous support of a number of agen-
424 cies and institutes that have supported the *Fermi* LAT Collaboration. These include the
425 National Aeronautics and Space Administration and the Department of Energy in the United
426 States, the Commissariat à l’Energie Atomique and the Centre National de la Recherche Sci-
427 entifique / Institut National de Physique Nucléaire et de Physique des Particules in France,
428 the Agenzia Spaziale Italiana and the Istituto Nazionale di Fisica Nucleare in Italy, the
429 Ministry of Education, Culture, Sports, Science and Technology (MEXT), High Energy Ac-

430 celerator Research Organization (KEK) and Japan Aerospace Exploration Agency (JAXA)
431 in Japan, and the K. A. Wallenberg Foundation and the Swedish National Space Board in
432 Sweden. The Arecibo Observatory is part of the National Astronomy and Ionosphere Center,
433 which is operated by Cornell University under a cooperative agreement with the National
434 Science Foundation. The National Radio Astronomy Observatory is a facility of the National
435 Science Foundation Operated under cooperative agreement by Associated Universities, Inc.
436 Support for this work was provided by the National Aeronautics and Space Administration
437 through *Chandra* Award Number GO6-7136X issued by the *Chandra* X-Ray Observatory
438 Center, which is operated by the Smithsonian Astrophysical Observatory for and on behalf
439 of NASA under contract NAS8-03060. This research has made use of software provided
440 by the *Chandra* X-Ray Center in the application package CIAO. This research has made
441 use of data obtained from the High Energy Astrophysics Science Archive Research Center
442 (HEASARC), provided by NASA’s Goddard Space Flight Center.

443 REFERENCES

- 444 Abdo, A. A. et al. 2009a, *Science*, 325, 840, (Blind Search Pulsars)
- 445 —. 2009b, *ApJS*, 183, 46, (Bright Source List)
- 446 —. 2009c, in prep (1st Fermi LAT Gamma-Ray Catalog)
- 447 —. 2009d, Submitted to *ApJ* (Fermi Catalog of Gamma-ray Pulsars)
- 448 —. 2007, *ApJ*, 664, L91, (The Milagro Collaboration)
- 449 Aharonian, F. et al. 2009, *A&A*, 499, 723
- 450 —. 2006, *A&A*, 460, 365
- 451 Atwood, W. B. et al. 2009, *ApJ*, 697, 1071, (LAT)
- 452 Blondin, J. M., Chevalier, R. A., & Frierson, D. M. 2001, *ApJ*, 563, 806
- 453 Camilo, F. et al. 2009, *ApJ*, in press (arXiv:0908.2626) - Radio detection of two gamma-ray
454 pulsars
- 455 Chatterjee, S. et al. 2009, *ApJ*, 698, 250
- 456 —. 2005, *ApJ*, 630, L61
- 457 Cordes, J. M. et al. 2006, *ApJ*, 637, 446

- 458 Cordes, J. M., & Lazio, T. J. W. 2002, ArXiv e-prints, (arXiv:astro-ph/0207156)
- 459 de Jager, O. C. 2008, ApJ, 678, L113
- 460 Deller, A. T., Tingay, S. J., Bailes, M., & Reynolds, J. E. 2009, ApJ, 701, 1243
- 461 Dickey, J. M., & Lockman, F. J. 1990, ARA&A, 28, 215
- 462 Dowd, A., Sisk, W., & Hagen, J. 2000, in Astronomical Society of the Pacific Conference Series, Vol. 202, IAU Colloq. 177: Pulsar Astronomy - 2000 and Beyond, ed. M. Kramer,
463 N. Wex, & R. Wielebinski, 275
- 464
- 465 Downes, A. J. B., Salter, C. J., & Pauls, T. 1980, A&A, 92, 47
- 466 Ferreira, S. E. S., & de Jager, O. C. 2008, A&A, 478, 17
- 467 Frail, D. A., Giacani, E. B., Goss, W. M., & Dubner, G. 1996, ApJ, 464, L165+
- 468 Gaensler, B. M., Stappers, B. W., Frail, D. A., & Johnston, S. 1998, ApJ, 499, L69+
- 469 Gonthier, P. L., Van Guilder, R., & Harding, A. K. 2004, ApJ, 604, 775
- 470 Hartman, R. C. et al. 1999, ApJS, 123, 79
- 471 Haslam, C. G. T., Salter, C. J., Stoffel, H., & Wilson, W. E. 1982, A&AS, 47, 1
- 472 Hobbs, G., Edwards, R., & Manchester, R. 2006, Chinese Journal of Astronomy and Astro-
473 physics Supplement, 6, 189
- 474 Kaspi, V. M., Roberts, M. E., Vasisht, G., Gotthelf, E. V., Pivovarov, M., & Kawai, N.
475 2001, ApJ, 560, 371
- 476 Kaspi, V. M., Roberts, M. S. E., & Harding, A. K. 2006, in Compact stellar X-ray sources,
477 ed. W. H. G. Lewin & M. van der Klis, 279–339
- 478 Lamb, R. C., & Macomb, D. J. 1997, ApJ, 488, 872
- 479 Langston, G., Minter, A., D’Addario, L., Eberhardt, K., Koski, K., & Zuber, J. 2000, AJ,
480 119, 2801
- 481 Ransom, S. M., Eikenberry, S. S., & Middleditch, J. 2002, AJ, 124, 1788
- 482 Ray, P. S., et al. 2009, ApJ, in prep (Precise Timing of Fermi Gamma-Ray Pulsars)
- 483 Roberts, M. S. E., Romani, R. W., & Kawai, N. 2001, ApJS, 133, 451

- 484 Romani, R. W., & Yadigaroglu, I.-A. 1995, ApJ, 438, 314
- 485 Russeil, D. 2003, A&A, 397, 133
- 486 Stil, J. M. et al. 2006, AJ, 132, 1158
- 487 Ward, J. E. 2008, in American Institute of Physics Conference Series, Vol. 1085, American
488 Institute of Physics Conference Series, ed. F. A. Aharonian, W. Hofmann, & F. Rieger,
489 301–303
- 490 Watters, K. P., Romani, R. W., Weltevrede, P., & Johnston, S. 2009, ApJ, 695, 1289
- 491 Yang, J., Zhang, J.-L., Cai, Z.-Y., Lu, D.-R., & Tan, Y.-H. 2006, Chinese Journal of Astron-
492 omy and Astrophysics, 6, 210

493

Table 1: Measured and Derived timing parameters of PSR J1907+0602

Fit and data-set	
Pulsar name	J1907+0602
MJD range	54647–55074
Number of TOAs	23
Rms timing residual (μs).....	404
Measured Quantities	
Right ascension, α	19:07:54.71(14)
Declination, δ	+06:02:16.1(23)
Pulse frequency, ν (s^{-1})	9.3780713067(19)
First derivative of pulse frequency, $\dot{\nu}$ (s^{-2}) ..	$-7.6382(4) \times 10^{-12}$
Second derivative of pulse frequency, $\ddot{\nu}$ (s^{-3})	$2.5(6) \times 10^{-22}$
Epoch of frequency determination (MJD) ..	54800
Dispersion measure, DM ($cm^{-3}pc$)	82.1(11)
Derived Quantities	
Characteristic age (kyr)	19.5
Surface magnetic field strength (G)	3.1×10^{12}
\dot{E} ($erg\ s^{-1}$)	2.8×10^{36}
Assumptions	
Time units	TDB
Solar system ephemeris model.....	DE405

Note. — The numbers in parentheses are the errors in the last digit of the fitted parameters. The errors are statistical only, except for the position error, as described in §2. The derived parameters of \dot{E} , B , and τ_c are essentially unchanged with respect to those reported by (Abdo et al. 2009a), but the position has moved by 1.2 arcmin.

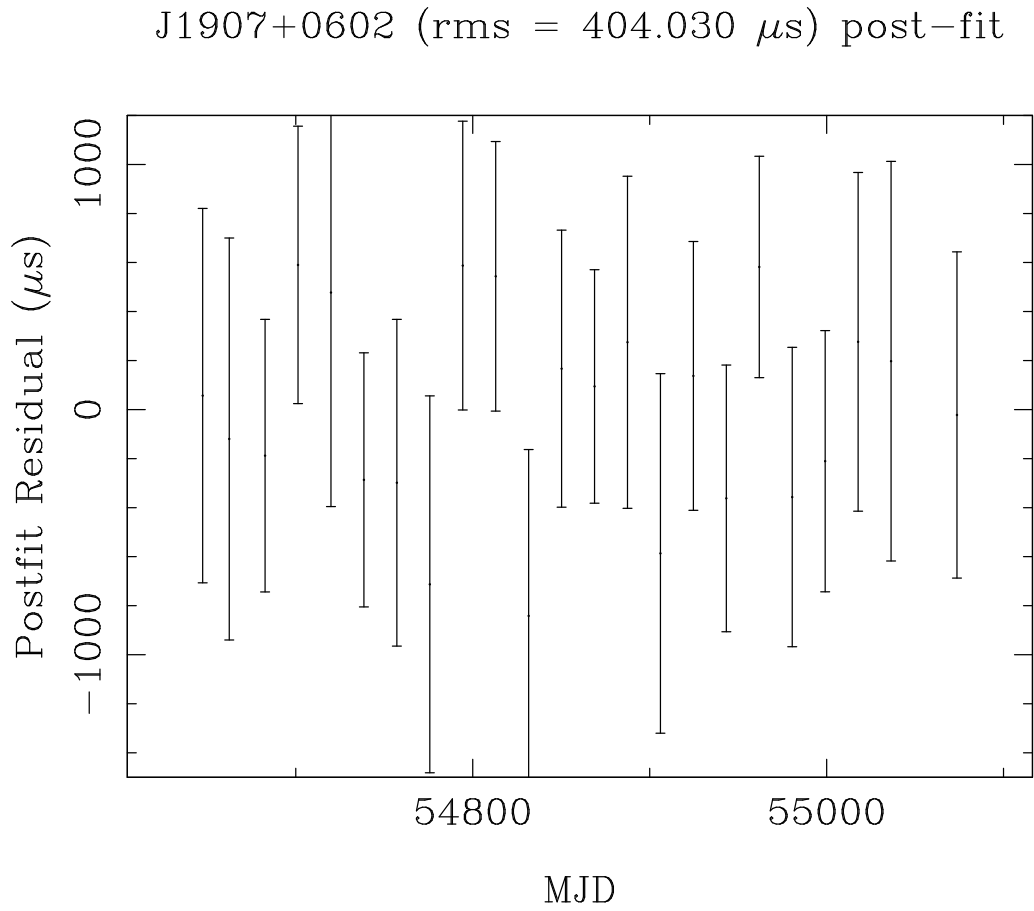


Fig. 1.— Post-fit timing residuals for PSR J1907+0602. The reduced chi-square of the fit is 0.5.

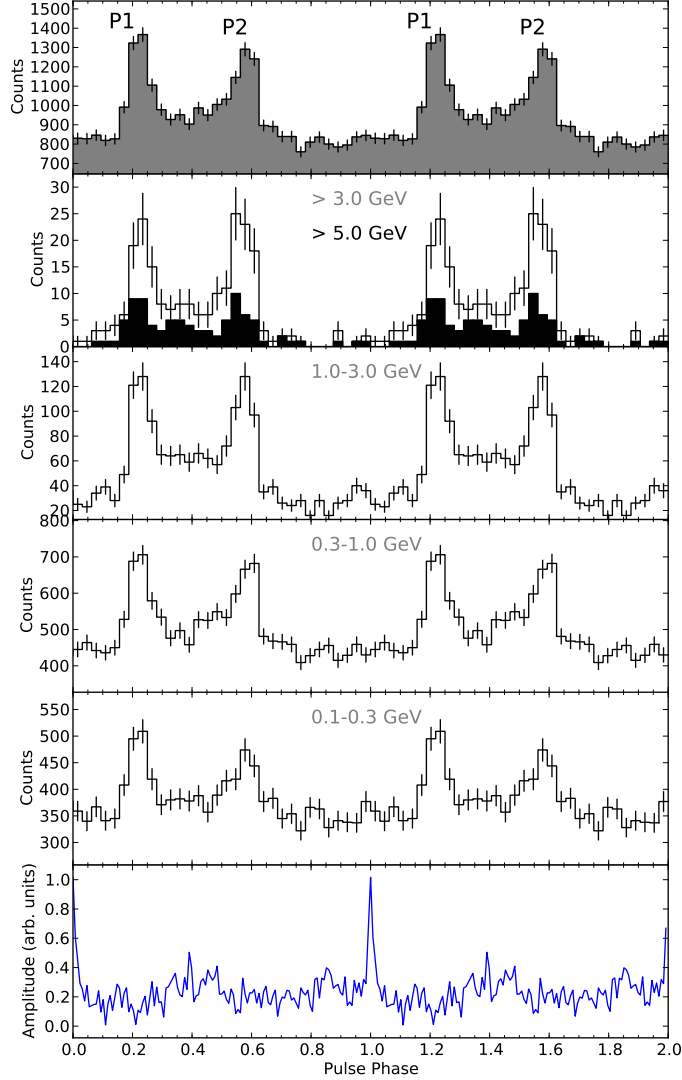


Fig. 2.— Folded light curves of PSR J1907+0602 in 32 constant-width bins for different energy bands and shown over two pulse periods with the 1.4 GHz radio pulse profile plotted in the bottom panel. The top panel of the figure shows the folded light curve for photons with $E > 0.1$ GeV. The other panels show the pulse profiles in exclusive energy ranges: $E > 3.0$ GeV (with $E > 5.0$ GeV in black) in the second panel from the top; 1.0 to 3.0 GeV in the next panel; 0.3 to 1.0 GeV in the fourth panel; and 0.1 to 0.3 GeV in the fifth panel.

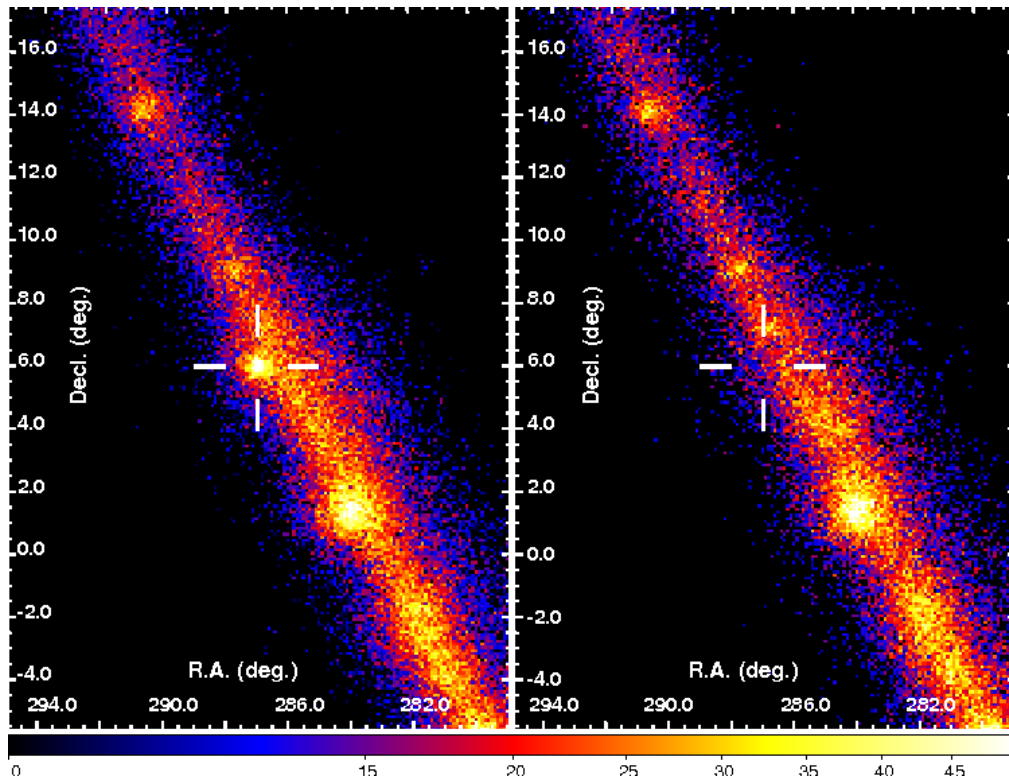


Fig. 3.— The observed *Fermi*-LAT counts map of the region around PSR J1907+0602. Left: “on” pulse image, right: “off” pulse image. The open cross-hair marks the location of the pulsar. Color scale shows the counts per pixel.

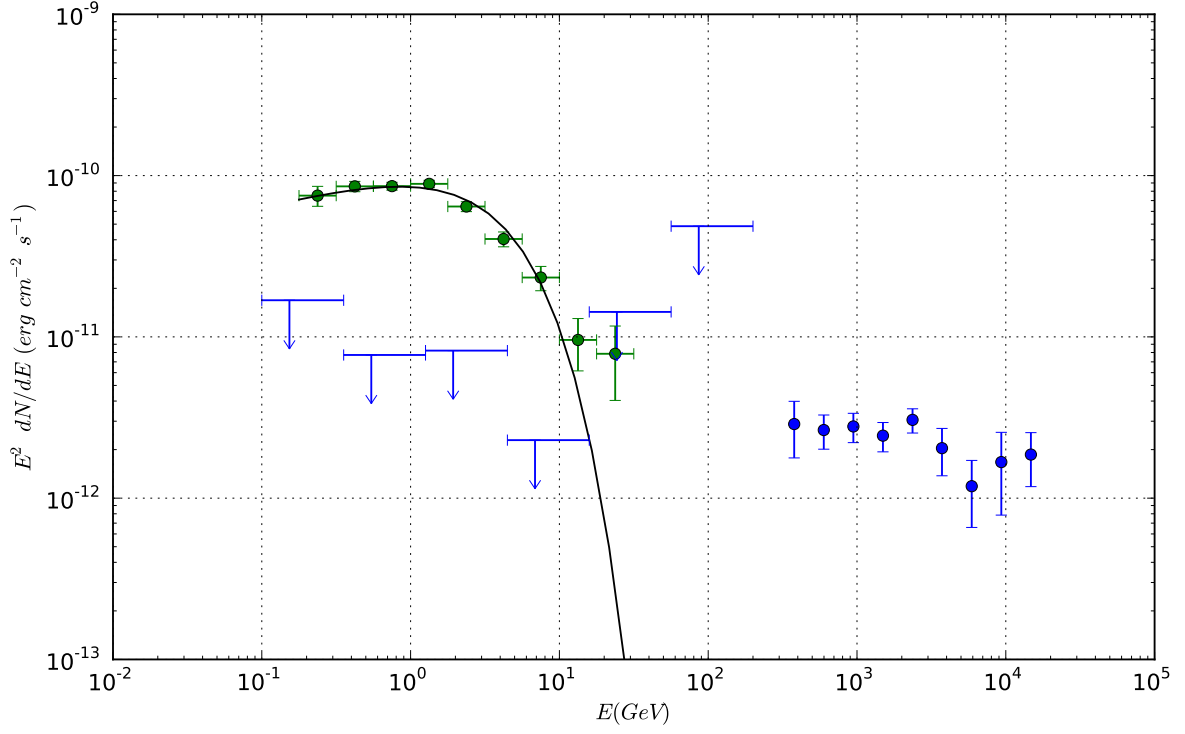


Fig. 4.— Phase-averaged spectral energy distribution for PSR J1907+0602 (green circles). Blue circles are data from HESS for HESS J1908+063 TeV source. 2σ upper limits from Fermi for emission from this TeV source are shown in blue. The black line shows the spectral model for the pulsar (equation 1). The upper limits suggest that the spectrum of HESS J1908+063 has a low energy turnover between 20 GeV and 300 GeV.

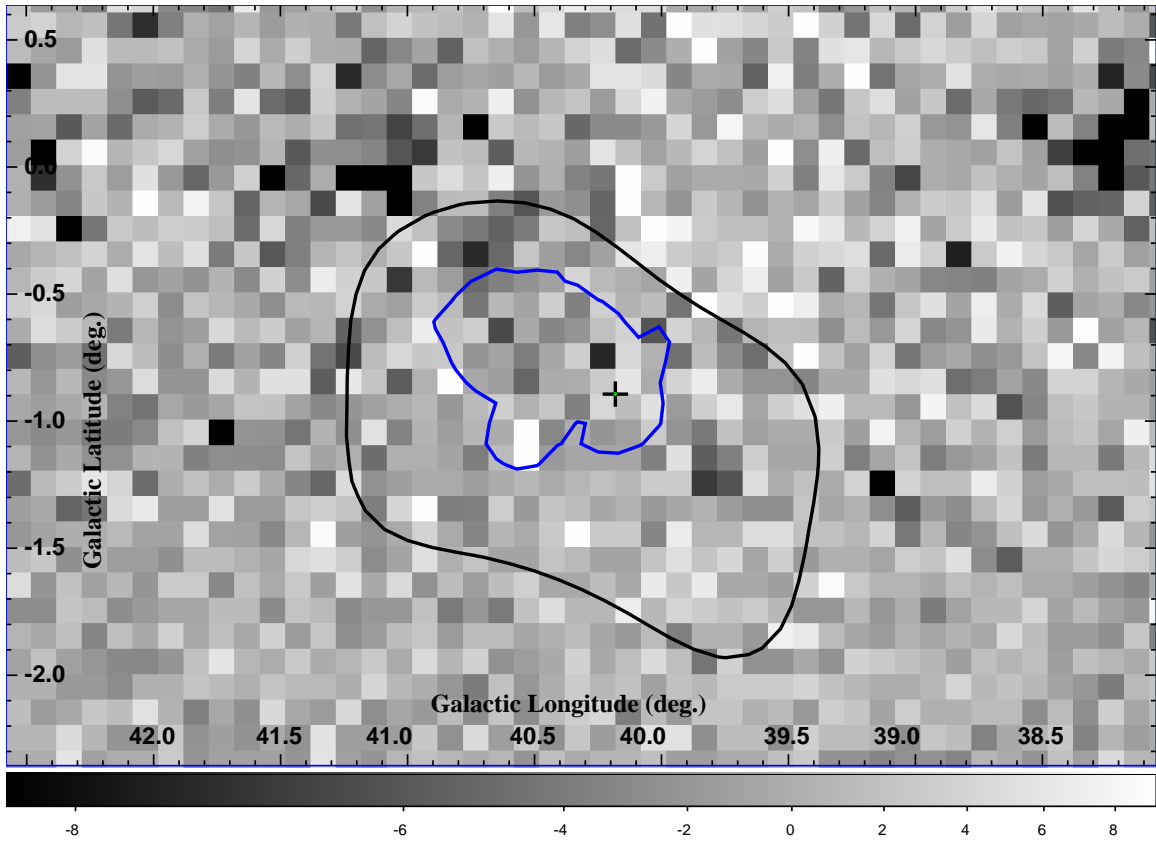


Fig. 5.— Residual map of the region around PSR J1907+0602 in the off-pulse. The timing position of the pulsar is marked by the cross. The 5σ contours from Milagro (outer) and HESS (inner) are overlaid.

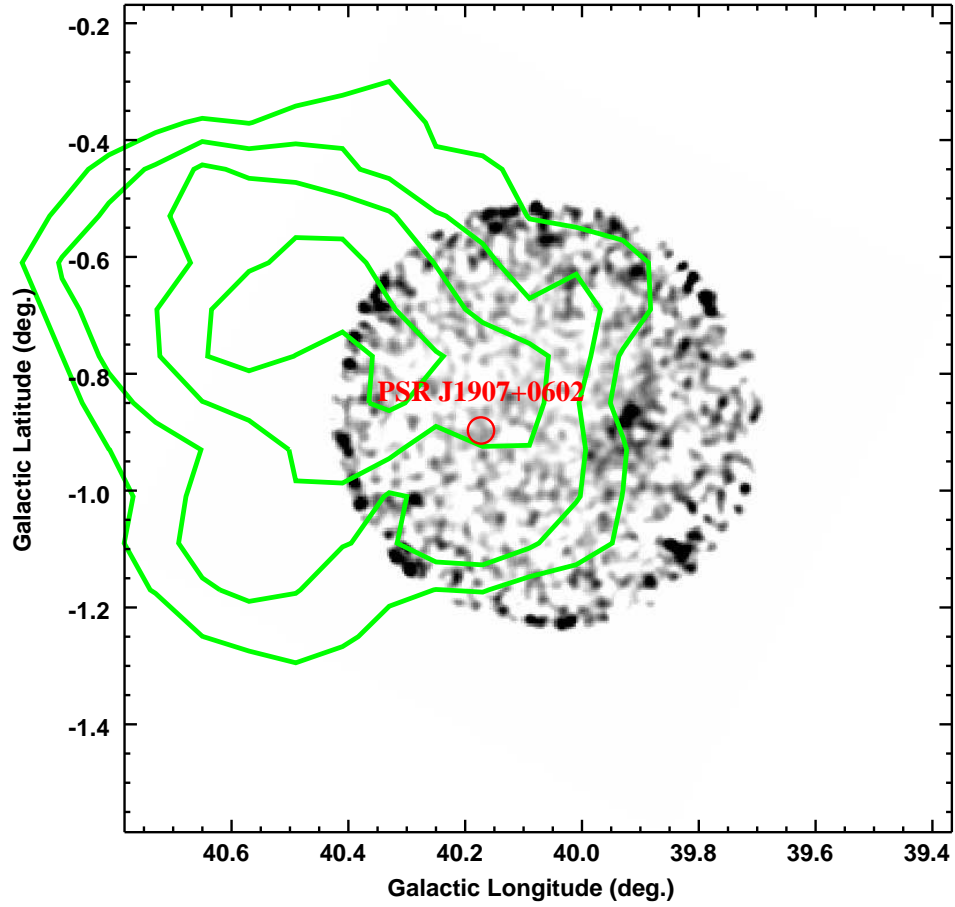


Fig. 6.— *ASCA* GIS 2-10 keV image of the region around PSR J1907+0602. The green contours are the 4-7 σ significance contours from HESS.

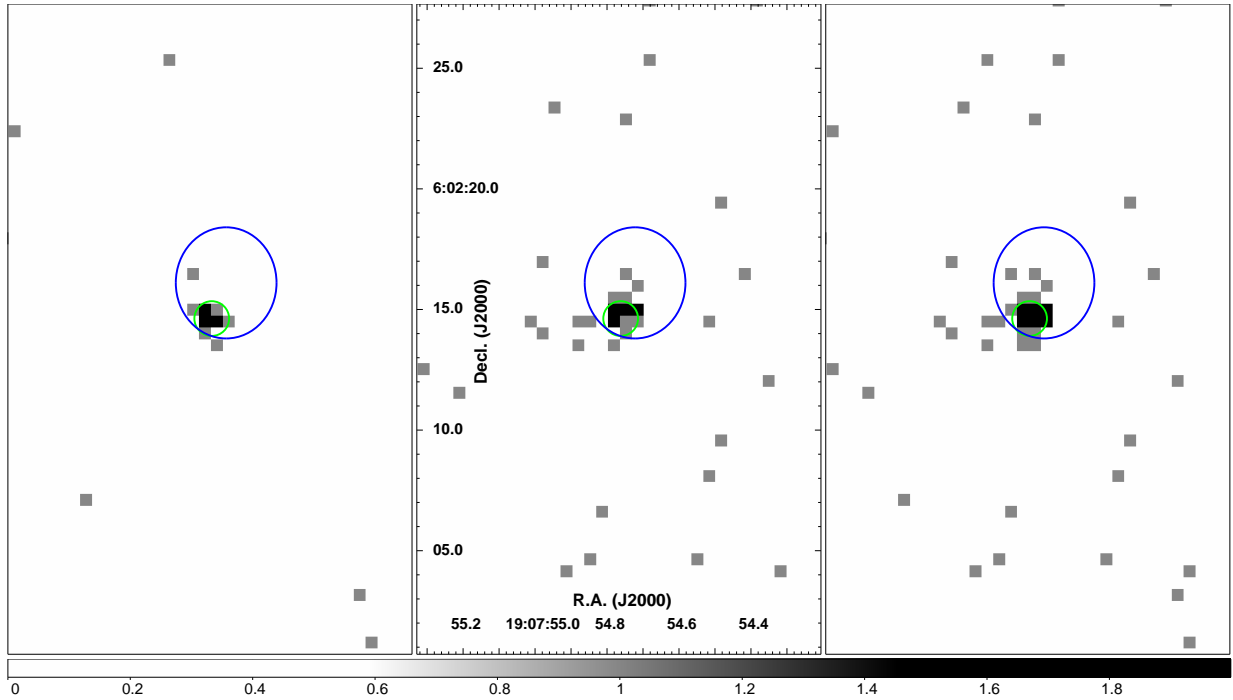


Fig. 7.— *Chandra* ACIS images of PSR J1907+0602. The blue ellipse shows the uncertainty in the timing position. The green circle of radius $0.8''$ is twice the FWHM of the 5keV PSF at this position, and should contain roughly 80% of the counts. The image at 0.75-2 keV (Left), 2-8 keV (Center) and 0.75-8 keV (right) is shown. Color scale shows the counts per pixel.

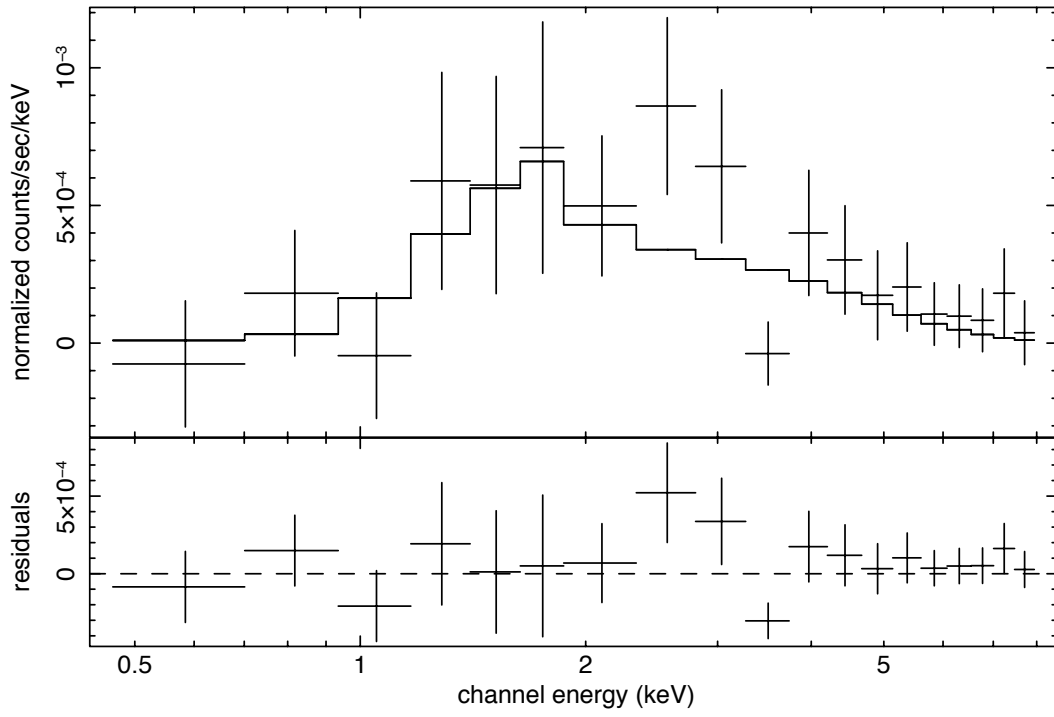


Fig. 8.— *Chandra* X-ray spectrum of PSR J1907+0602.

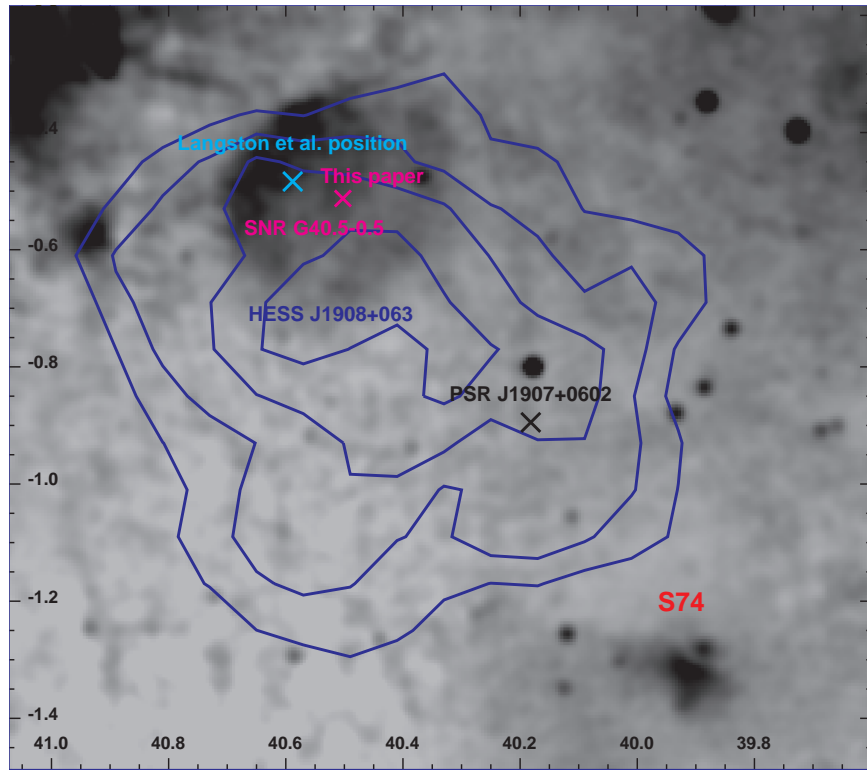


Fig. 9.— VGPS 1420 MHz image of region in Galactic coordinates showing relationship between SNR G40.5–0.5, HESS J1907+063 (blue contours representing the 4,5,6 and 7 σ significance levels), the star forming region S74, and PSR J1907+0602.